Refractive Guide Switching a Regenerative Amplifier Free-Electron Laser for High Peak and Average Power Hard X Rays

Gabriel Marcus,* Alex Halavanau, Zhirong Huang, Jacek Krzywinski, James MacArthur, Rachel Margraf, Tor Raubenheimer, and Diling Zhu
SLAC National Accelerator Laboratory, Menlo Park, California 94025, USA

(Received 15 July 2020; revised 30 October 2020; accepted 10 November 2020; published 18 December 2020)

We present an x-ray regenerative amplifier free-electron laser design capable of producing fully coherent hard x-ray pulses across a broad tuning range at a high steady state repetition rate. The scheme leverages a strong undulator taper and an apertured diamond output-coupling cavity crystal to produce both high peak and average spectral brightness radiation that is 2 to 3 orders of magnitude greater than conventional single-pass self-amplified spontaneous emission free-electron laser amplifiers. Refractive guiding in the postsaturation regime is found to play a key role in passively controlling the stored cavity power. The scheme is explored both analytically and numerically in the context of the Linac Coherent Light Source II High Energy upgrade.

DOI: 10.1103/PhysRevLett.125.254801

The emergence of x-ray free-electron lasers (XFELs) that generate ultrashort x-ray pulses with a billionfold increase in peak brightness relative to third generation synchrotrons is transforming many fields of science [1]. Indeed, the global XFEL capacity has increased significantly in response to the demand for the unique capabilities offered by these new sources [2–7]. These facilities are largely based on single-pass self-amplified spontaneous emission (SASE) [8,9] and result in transversely coherent x-ray pulses with stochastic temporal and spectral structures [10]. The realization of a true x-ray laser, one that generates fully coherent and stable x-ray beams, will drive another qualitative advance for many areas of science. In particular, an x-ray source capable of simultaneously delivering both high peak and average spectral brightness pulses promises to open new areas of science using, for instance, x-ray photon correlation spectroscopy to characterize spontaneous fluctuations and materials heterogeneity in the time domain [11,12]. A high average power and fully coherent x-ray source will significantly enhance the ability to distinguish structural changes in short time intervals at the atomic scale, which scales inversely with the square of the beam brightness [13]. Significant additional advances in coherent diffractive imaging, single-particle imaging, nonlinear x-ray optics, nonlinear x-ray spectroscopy, and x-ray quantum optics will also be made possible by a high peak and average brightness source [14–20].

Cavity-based XFELs [21] such as the x-ray regenerative amplifier free-electron laser (XRAFEL) [22,23] have seen renewed interest as a means of producing, amplifying, and delivering fully coherent and stable hard x-ray pulses. This scheme relies on a high-brightness electron bunch supporting free-electron laser (FEL) gain in an undulator, while an x-ray cavity monochromatizes and recirculates x-ray radiation to interact with following fresh electron bunches. The XRAFEL operates as a high-gain FEL that targets the production of short ($\lesssim$ 100 fs) but high peak power x-ray pulses and can generally use the same electron beam employed in conventional single-pass SASE amplifiers. Of particular interest here is the output coupling efficiency of the x-ray cavity optics, which, as a consequence of the high-gain operation, can be large (often $> 99\%$). Therefore, the XRAFEL can operate as a source for both high peak and average brightness fully coherent hard x-rays.

High-gain FEL systems can often use strong undulator tapering to push the conversion efficiency of electrical to optical power well beyond the nominal saturation limit [24–28]. This process is optimized for systems that harness strong optical seeds to interact with fresh electron bunches, which an XRAFEL would excel at delivering. However, output coupling a significant fraction of the stored cavity x-ray radiation remains a challenge. The cavity diamond Bragg mirrors—used for their radiation hardness and superior optical, thermal, and mechanical properties—have record high reflectivity within the narrow cavity bandwidth [29–32]. Both active [33] and passive output-coupling modalities [34–36] are currently under investigation and include studies of both x-ray cavity optics and electron bunch manipulations. In this Letter, we present a new passive output coupling scheme that exploits the third cavity-based x-ray free-electron laser ingredient: the undulator. We show that optical guiding in a static but strongly tapered undulator can produce both a high peak and average brightness x-ray source. The scheme as depicted in Fig. 1 and described below relies on an apertured output-coupling diamond crystal that passively returns an ever

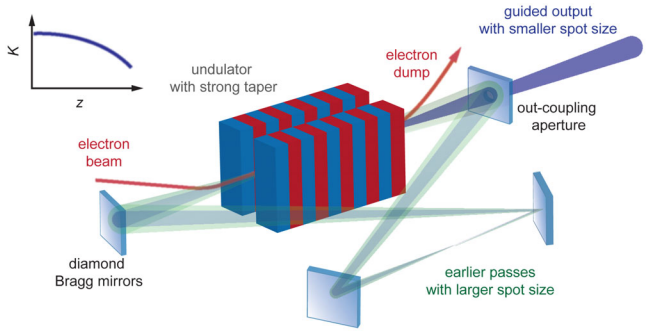

FIG. 1. Schematic of the refractive guide switching scheme.

smaller fraction of the stored cavity energy as the system evolves from noise. The undulator taper drives the FEL efficiency significantly past the saturation limit upon reaching a steady operating state in as few as five passes, while the apertured diamond optic transmits ~95–99% of the x-ray power.

Optical guiding in an FEL has been studied in detail and generally separates into two distinct effects, gain guiding and refractive guiding [37–46]. These effects can be distinguished based on the notion of a complex refractive index for an axially symmetric electron beam having a Gaussian transverse profile [42]:

$$n(r,z,A) = 1 + \frac{1}{2}\frac{\omega_b^2(r,z)}{\omega^2}\left\langle \frac{e^{i\psi}}{\gamma}\right\rangle \frac{K[JJ]}{|A(r,z)|}. \quad (1)$$

Here, $\omega_b^2(r,z) = \omega_{b0}^2[r_{b0}/r_b(z)]^2 \exp[-r^2/r_b^2(z)]$, $r_b(z)$ is the electron-beam radius, $r_{b0} = r_b(0)$, $\omega_{b0} = (n_0 e^2/m\epsilon_0)^{1/2}$ is the initial beam plasma frequency on axis, n_0 is the initial density on axis, $K = eB_u/k_u mc$ is the normalized vector potential of a planar undulator, B_u is the undulator magnetic field strength on axis, $k_u = 2\pi/\lambda_u$, λ_u is the undulator period, $[JJ]$ is the Bessel factor associated with planar undulators [47], $A = eE_r/kmc^2$ is the normalized vector potential of the electric field E_r, $\omega = ck$ is the radiation frequency, γ is the electron's Lorentz factor, ψ is the electron's phase in the ponderomotive potential formed by the undulator and x-ray electric fields, and $<>$ denotes an ensemble average over the electrons.

We are primarily concerned with the effects of refractive guiding, which is associated with the real part of the complex index of refraction, in the postsaturation and strongly tapered regime. The development of bunching in the FEL shifts the radiation frequency so that the copropagating radiation experiences a local index of refraction that is greater than 1. The bunched beam therefore acts like an optical fiber, confining the radiation near the beam axis.

A simple analogy to a quadratic graded refractive index medium is instructive here, while a detailed self-consistent model of optical guiding will be explored in a separate publication. Consider the x-ray radiation to be approximated by a lowest order transverse Gaussian mode,

$$A(r,z) = A_0(z)\exp\{-[1 - i\alpha(z)]r^2/r_s^2(z)\}, \quad (2)$$

where r_s is the spot size and $\alpha(z)$ is related to the inverse of the radius of curvature of the radiation. Inserting this field into Eq. (1), expanding the result to second order in r, and taking the real part yields

$$\mathrm{Re}[n(r,z,A)] \approx 1 + \chi - \chi\left(\frac{1}{r_b^2} - \frac{1}{r_s^2}\right)r^2 = n_0 - \frac{1}{2}n_2 r^2, \quad (3)$$

where $\chi = 2c^2\nu K[JJ]/(\omega^2|A_0|r_b^2)\langle\cos(\psi)/\gamma\rangle$, $\nu = \omega_{b0}^2 r_{b0}^2/4c^2 = I_b/I_A$ is Budker's constant, I_b is the electron beam current, and I_A is the Alfvén current. An index of refraction as described in Eq. (3) can support a stable trapped Gaussian eigenmode of size [48]

$$r_s^2 = \frac{\lambda}{\pi\sqrt{n_2}}. \quad (4)$$

n_2 can be simplified further in the tapered postsaturation regime by making the resonant particle approximation [24], where the phase of the electrons that are trapped in the ponderomotive bucket in a tapered FEL all have $\psi \approx \psi_r$ and $\gamma \approx \gamma_r = [k(1 + K^2/2)/2k_u]^{1/2}$ so that $\langle\cos(\psi)/\gamma\rangle \approx f_t\cos(\psi_r)/\gamma_r$. f_t is the trapped electron fraction. The resonant phase is determined by both the rate of change in the undulator magnetic field and the amplitude of the radiation field via $\sin(\psi_r) = -K'/(2k_u A[JJ])$, where the prime denotes a derivative in z. Furthermore, for small FEL and taper efficiencies $K/\gamma \approx K_0/\gamma_0$ and we can simplify n_2 as

$$n_2 = \frac{4c^2}{\omega^2}\nu f_t\cos\psi_r\frac{K_0}{\gamma_0}\frac{1}{|A_0|r_b^2}\left(\frac{1}{r_b^2} - \frac{1}{r_s^2}\right). \quad (5)$$

Equation (5) indicates that it is important to keep the trapped fraction of electrons, $0 < f_t < 1$, and therefore the electron bunching, large throughout tapered FEL amplification to keep the confined eigenmode size, r_s, matched to the electron beam.

The refractive guide switching scheme for an XRAFEL proceeds as follows. A strong undulator taper is implemented with an apertured output-coupling diamond crystal of fixed diameter D. The taper is ideally matched to a particular seed power P_0 that generates strong bunching prior to saturation and maintains this bunching throughout postsaturation refractive guided amplification. Seed powers lower than P_0, however, are not matched well to the taper. Electrons will detrap from their ponderomotive buckets and will no longer support refractive guiding or amplification. The unguided radiation in this case will have a larger spot size on the output-coupling crystal and the cavity will return a larger fractional pulse energy for seeding. As the

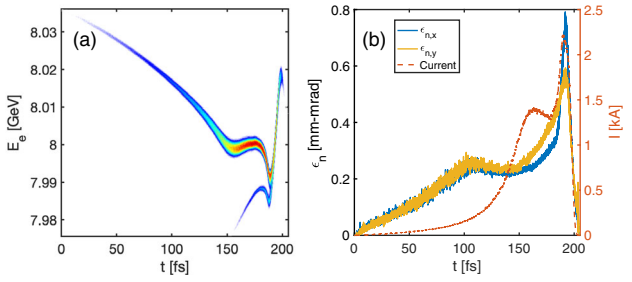

FIG. 2. Start-to-end properties of a 100 pC charge electron bunch (head is to the right). Unless otherwise noted, solid lines correspond to the left vertical axis and dashed lines to the right. (a) Longitudinal phase space. (b) Current profile (red, dashed) and slice emittance (solid).

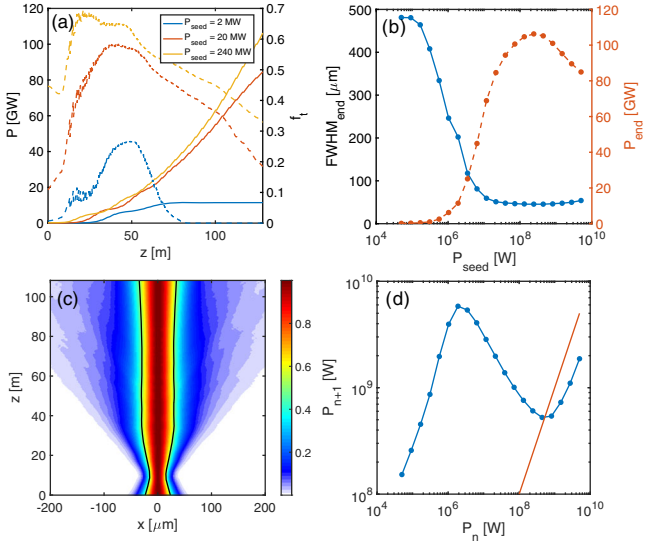

FIG. 3. Single-frequency XRAFEL simulations at $E_{\mathrm{ph}} = 10$ keV. (a) Power gain curves (solid) and trapped electron fraction (dashed) along the undulator for three representative seed powers. (b) FWHM radiation size (solid) and power (dashed) at the exit of the undulator vs seed power. (c) Normalized projected intensity evolution along the undulator for $P_{\mathrm{seed}} = 240$ MW. The black lines are 0.5 contours. (d) Seed power at a following pass $(n+1)$ assuming a seed power at a given pass (n) (blue) assuming a circular aperture of diameter $D = 200$ μm. The red line indicates possible equilibrium points.

seed power increases from pass to pass, the taper becomes more effective, the electrons are trapped longer and support refractive guiding and amplification, and the aperture returns a smaller fractional pulse energy until a steady state is reached. This passive output-coupling scheme dynamically changes the radiation output-coupling fraction to ensure that early passes return a large enough seed power to dominate shot noise while later passes transmit most of the pulse energy and keep the stored cavity power to a manageable level. We explore this scheme below with numerical particle simulations using the FEL code GENESIS [49] within the context of the Linac Coherent Light Source II High Energy (LCLS-II-HE) project.

The LCLS-II-HE project [50] is a high energy upgrade to the 4 GeV superconducting radio-frequency linear accelerator currently being installed at SLAC as part of the LCLS-II project [51]. It will produce electron beams with an energy of 8 GeV and will be capable of operating at ~MHz repetition rates, making realistic x-ray cavity footprints (~300 m round-trip distance) feasible.

A representative electron bunch longitudinal phase space, as well as slice emittance and current profiles, can be found in Fig. 2 for a 100 pC charge bunch. The core of this distribution (from ~120–200 fs) is used to define the parameters for single-frequency simulations and also for three-dimensional start-to-end simulations. The linearly polarized undulator consists of 32 gap-tunable segments of 130 periods each, which are interspersed with strong focusing quadrupoles. The maximum undulator $K_{\mathrm{max}} = 2.44$ and has a period $\lambda_u = 26$ mm.

We first study optical guiding in a strongly seeded FEL interaction, which is characteristic of an XRAFEL system. The process is investigated using single-frequency simulations at $E_{\mathrm{ph}} = 10$ keV for a fixed but strong undulator taper [52–54] by varying the seed power while keeping the seed Rayleigh length (10 m) and waist location (10 m into the undulator) fixed.

Figure 3(a) shows the gain curves and trapping fraction for three seed powers representing the low, moderate, and nearly optimized cases. The trapping fraction is largest, the radiation power achieves a faster growth rate, and the final power is maximized as the seed power is increased toward a nearly optimized value of ~240 MW. The increase in trapping fraction and final power at the undulator exit, which results from increasing the seed power from low levels toward an optimized value, should also result in a corresponding smaller final spot size as refractive guiding is better maintained throughout amplification. This is clearly illustrated in Fig. 3(b), which shows the radiation FWHM transverse size and final power at the end of the undulator as a function of seed power. An optimal seed power of $\sim P_0 = 200$ MW produces an FWHM transverse size of ~50 μm and a power at the end of the undulator of ~100 GW. Figure 3(c) shows the evolution of the horizontally projected transverse intensity normalized to its peak value along the undulator for this case. The FWHM spot size, indicated by the black contours, maintains a nearly constant value along the undulator in the postsaturation regime. The core of the radiation is clearly guided while a small fraction of the total radiation leaks outside of the electron beam as the trapped fraction decreases. Finally, a simple model for the system stability can be found by considering an outcoupling aperture of fixed diameter D and lossless cavity optics that return the radiation to the same initial transverse conditions. Figure 3(d) shows a map that returns the seed power at pass $n+1$ given a seed power at pass n under the above

TABLE I. XRAFEL performance and diamond Bragg mirror parameters.

E [keV]	Miller indices	D [μm]	Photons per pulse	$\Delta E/E$	Δt [fs]	B_{avg} [a]	B_{peak} [a]
5.875	(311)	200	9.0×10^{12}	2.5×10^{-5}	40	3.3×10^{28}	8.1×10^{35}
10.0	(440)	200	2.1×10^{12}	1.5×10^{-5}	40	3.8×10^{28}	9.4×10^{35}
14.4	(733)	80	6.4×10^{10}	9.6×10^{-6}	40	3.8×10^{28}	9.6×10^{35}
20.0	(880)	40	1.3×10^{10}	1.0×10^{-5}	20	1.3×10^{27}	6.4×10^{34}

[a]photons/ sec /(mm-mrad)^2/(0.1%bandwidth).

stated conditions for $D = 200$ μm. The intersection of the map with the line $P_{n+1} = P_n$ is an equilibrium point. The slope of the map near this intersection is nearly zero, indicating it is a stable equilibrium.

Stable and fixed transverse seed radiation properties cannot be maintained, however, as the real system develops from noise, the effective radiation source properties in the undulator evolve from pass to pass, and the output-coupling aperture impacts the radiation distribution. Therefore, time-dependent and three-dimensional multipass XRAFEL simulations have been performed using the electron beam in Fig. 2 beginning from noise at photon energies of 5.87,10.0,14.4, and 20.0 keV. The 3D radiation field at the end of the undulator was propagated through a 300 m round-trip length (1 MHz electron beam repetition rate) optical cavity that adopts the geometry proposed in [55,56] (see Fig. 1). The cavity is formed by four 500 μm thick diamond crystals, the first of which has a circular aperture of diameter D. The aperture diameter has been empirically optimized and depends on the resonant photon energy (see Table I). Two compound refractive lenses placed symmetrically about the undulator midpoint and having focal lengths of $f \sim 150$ m provide stable cavity eigenmode waist locations in the middle of the undulator and 150 m away in the return line. Fourier optics techniques [57] are used for x-ray free-space propagation and the compound refractive lens focusing, while the dynamical theory of x-ray Bragg diffraction is used to model the interaction of the recirculated cavity x-rays with the diamond Bragg mirrors [58].

We illustrate the performance at $E_{ph} = 10.0$ keV in Fig. 4. Twenty-five independent XRAFEL runs seeded only by shot noise were performed until a steady state was reached after ~11 passes. The average seed (amplified) pulse energy as well as rms fluctuations as a function of pass number can be found in Fig. 4(a), (b). An extremely stable steady state operation is reached after ~6 passes at an amplified pulse energy of ~3.5 mJ (0.2% relative rms fluctuations) and a returned energy fraction <1%. Figure 4(c) shows the longitudinal phase space of the spent electron beam at the end of the 11th pass as well as the temporal x-ray power profile. Only ~16% of the electrons are trapped, indicating possible room for taper improvement. Nevertheless, the peak power of the radiation at the end of the undulator reaches over 100 GW, which represents a gain of ~12 over saturation and is in excellent agreement with single-frequency predictions. This radiation, however, is not Fourier transform limited as the combination of resistive wall wakefields in the undulator [59], initial electron bunch phase space curvature, and differential FEL gain along the longitudinal profile conspire to drive the accumulation of higher order temporal phase during FEL amplification. Furthermore, a small leading radiation spike drives interference fringes outside the main amplifying spectral spike. These effects are clearly evident in the on-axis far-field Wigner distribution and projections in Fig. 4(d). The radiation can be spectrally cleaned by a high efficiency postundulator monochromator in much the same way the x-ray cavity monochromatizes the returned x-rays for seeding. We note, however, that these effects are not fundamental limitations of the scheme and can be addressed by further electron bunch longitudinal phase space optimization. Similar performance simulations were

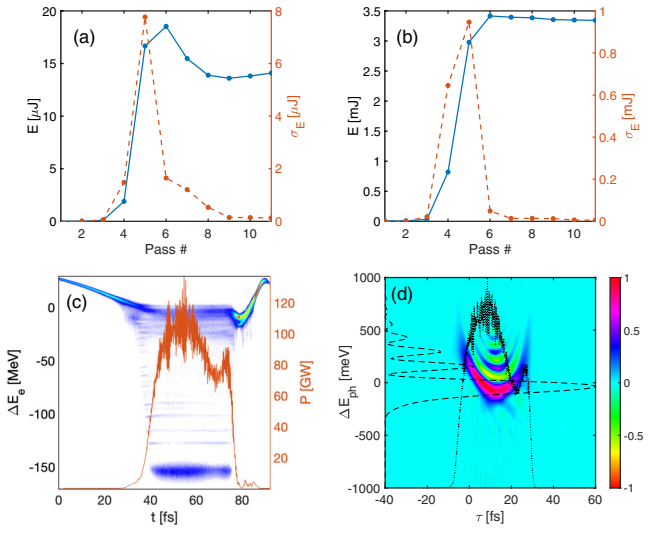

FIG. 4. XRAFEL simulations at $E_{ph} = 10.0$ keV. (a) Average seed energy (solid) and rms fluctuations (dashed) vs pass number. (b) Average amplified energy (solid) and rms fluctuations (dashed) vs pass number. (c) Representative electron bunch longitudinal phase space at the end of the 11th pass and temporal power profile (red, right vertical axis). (d) Normalized Wigner distribution of the on-axis far-field intensity of the 11th pass. The vertical projection (dotted line) is the on-axis temporal intensity (arb. units), while the horizontal projection (dashed line) is the on-axis spectral intensity (arb. units).

completed for resonant photon energies of 5.87, 14.4, and 20.0 keV and are summarized in Table I. It should be noted that ~8.3 mJ of pulse energy and over 200 GW of peak power per pulse are generated at 5.87 keV. This x-ray source would produce an impressive ~8.3 kW of average x-ray power. Perhaps more importantly, however, is that the stored cavity power in this scenario is held to 100 W, which is much less than similar cavity-based FEL scenarios considered elsewhere [60]. The average (peak) spectral brightness is greater than $10^{28}(\sim 10^{36})$ photons/ sec /(mm-mrad)^2/ (0.1%bandwidth) across most of the tuning range. This represents a leap of 2 to 3 orders of magnitude over single-pass SASE amplifiers [61]. The performance begins to degrade at the highest photon energies where electron beam emittance effects strongly come into play. Nonetheless, the XRAFEL still reaches steady state operation after 15 passes and produces ~40 W of average x-ray power at $E_{\mathrm{ph}} = 20$ keV.

In summary, we have presented an XRAFEL scheme that leverages a strong undulator taper to drive the FEL significantly past the nominal saturation point and passively switch ever higher and more stable FEL power out of the x-ray cavity after only a few passes starting from noise. Refractive guiding in the postsaturation regime was studied analytically and numerically, illuminating the principle of refractive guide switching through a fixed aperture. These effects conspire to push the peak and average spectral brightness of the XRAFEL 2 to 3 orders of magnitude beyond any single-pass SASE amplifier and promises to open new areas of science that can leverage narrow bandwidth, high peak power, fully coherent, and stable radiation.

We thank J. Qiang for supplying the start-to-end electron beams used in simulation, and W. M. Fawley, C. Emma, D. Nguyen, K.-J. Kim, and Y. Shvyd'ko for many insightful discussions. This work was supported by the Department of Energy, Laboratory Directed Research and Development program at SLAC National Accelerator Laboratory under Contract No. DE-AC02-76SF00515.

*Corresponding author.
gmarcus@slac.stanford.edu

[1] C. Bostedt, S. Boutet, D. M. Fritz, Z. Huang, H. J. Lee, H. T. Lemke, A. Robert, W. F. Schlotter, J. J. Turner, and G. J. Williams, Rev. Mod. Phys. **88**, 015007 (2016).
[2] W. Ackermann *et al.*, Nat. Photonics **1**, 336 (2007).
[3] P. Emma *et al.*, Nat. Photonics **4**, 641 (2010).
[4] T. Ishikawa *et al.*, Nat. Photonics **6**, 540 (2012).
[5] H.-S. Kang *et al.*, Nat. Photonics **11**, 708 (2017).
[6] W. Decking *et al.*, Nat. Photonics **14**, 391 (2020).
[7] V. S. Paul Scherrer Institute (PSI), Technical Report PSI–10-04, 2010.
[8] A. M. Kondratenko and E. L. Saldin, Part. Accel. **10**, 207 (1980).
[9] R. Bonifacio, C. Pellegrini, and L. Narducci, Opt. Commun. **50**, 373 (1984).
[10] R. Bonifacio, L. De Salvo, P. Pierini, N. Piovella, and C. Pellegrini, Phys. Rev. Lett. **73**, 70 (1994).
[11] G. Grbel, G. Stephenson, C. Gutt, H. Sinn, and T. Tschentscher, Nucl. Instrum. Methods Phys. Res., Sect. B **262**, 357 (2007).
[12] Lehmkühler *et al.*, Proc. Natl. Acad. Sci. U.S.A. **117**, 24110 (2020).
[13] R. Schoenlein *et al.*, SLAC Report SLAC-R-1053, 2015.
[14] A. Aquila *et al.*, Struct. Dyn. **2**, 041701 (2015).
[15] Z. Sun, J. Fan, H. Li, and H. Jiang, Appl. Sci. **8**, 132 (2018).
[16] J. Szlachetko *et al.*, Sci. Rep. **6**, 33292 (2016).
[17] T. E. Glover *et al.*, Nature (London) **488**, 603 (2012).
[18] R. Röhlsberger, K. Schlage, B. Sahoo, S. Couet, and R. Rüffer, Science **328**, 1248 (2010).
[19] B. W. Adams, C. Buth, S. M. Cavaletto, J. Evers, Z. Harman, C. H. Keitel, A. Plffy, A. Picn, R. Rhlsberger, Y. Rostovtsev, and K. Tamasaku, J. Mod. Opt. **60**, 2 (2013).
[20] B. Adams *et al.*, arXiv:1903.09317.
[21] G. Marcus *et al.*, in *39th International Free-Electron Laser Conference (FEL'19), Hamburg, Germany, 2019* (Joint Accelerator Conferences Website (JACoW), 2019), pp. 282–287.
[22] Z. Huang and R. D. Ruth, Phys. Rev. Lett. **96**, 144801 (2006).
[23] B. W. J. McNeil, IEEE J. Quantum Electron. **26**, 1124 (1990).
[24] N. Kroll, P. Morton, and M. Rosenbluth, IEEE J. Quantum Electron. **17**, 1436 (1981).
[25] C. Emma, N. Sudar, P. Musumeci, A. Urbanowicz, and C. Pellegrini, Phys. Rev. Accel. Beams **20**, 110701 (2017).
[26] Y. Jiao, J. Wu, Y. Cai, A. W. Chao, W. M. Fawley, J. Frisch, Z. Huang, H.-D. Nuhn, C. Pellegrini, and S. Reiche, Phys. Rev. ST Accel. Beams **15**, 050704 (2012).
[27] C. Emma, K. Fang, J. Wu, and C. Pellegrini, Phys. Rev. Accel. Beams **19**, 020705 (2016).
[28] E. A. Schneidmiller and M. V. Yurkov, Phys. Rev. ST Accel. Beams **18**, 030705 (2015).
[29] T. Kolodziej *et al.*, J. Synchrotron Radiat. **25**, 1022 (2018).
[30] S. Stoupin and Y. V. Shvyd'ko, Phys. Rev. Lett. **104**, 085901 (2010).
[31] Y. V. Shvyd'ko, S. Stoupin, A. Cunsolo, A. H. Said, and X. Huang, Nat. Phys. **6**, 196 (2010).
[32] Y. Shvydko, V. Blank, and S. Terentyev, MRS Bull. **42**, 437444 (2017).
[33] J. Krzywinski, Y. Feng, A. Halavanau, Z. Huang, A. Kissas, J. MacArthur, G. Marcus, T. Sato, and D. Zhu, in *39th International Free-Electron Laser Conference (FEL'19), Hamburg, Germany, 2019* (Joint Accelerator Conferences Website (JACoW), 2019), pp. 282–287.
[34] H. P. Freund, P. J. M. van der Slot, and Y. Shvyd'ko, New J. Phys. **21**, 093028 (2019).
[35] Y. Shvyd'ko, Phys. Rev. Accel. Beams **22**, 100703 (2019).
[36] J. P. MacArthur, A. A. Lutman, J. Krzywinski, and Z. Huang, Phys. Rev. X **8**, 041036 (2018).
[37] G. T. Moore, Opt. Commun. **52**, 46 (1984).
[38] E. T. Scharlemann, A. M. Sessler, and J. S. Wurtele, Phys. Rev. Lett. **54**, 1925 (1985).
[39] M. Xie and D. A. Deacon, Nucl. Instrum. Methods Phys. Res., Sect. A **250**, 426 (1986).

[40] G. T. Moore, Nucl. Instrum. Methods Phys. Res., Sect. A **250**, 418 (1986).
[41] P. Sprangle, A. Ting, and C. M. Tang, Phys. Rev. Lett. **59**, 202 (1987).
[42] P. Sprangle, A. Ting, and C. M. Tang, Phys. Rev. A **36**, 2773 (1987).
[43] B. Hafizi, A. Ting, P. Sprangle, and C. M. Tang, Phys. Rev. Lett. **64**, 180 (1990).
[44] Z. Huang and K.-J. Kim, Nucl. Instrum. Methods Phys. Res., Sect. A **483**, 504 (2002).
[45] W. Fawley, Nucl. Instrum. Methods Phys. Res., Sect. A **375**, 550 (1996).
[46] K. Li and H. Deng, Appl. Phys. Lett. **113**, 061106 (2018).
[47] Z. Huang and K.-J. Kim, Phys. Rev. ST Accel. Beams **10**, 034801 (2007).
[48] A. E. Siegman, *Lasers* (University Science Books, Mill Valley, 1986).
[49] S. Reiche, Nucl. Instrum. Methods Phys. Res., Sect. A **429**, 243 (1999).
[50] T. O. Raubenheimer, SLAC Report No. SLAC-R-1098, USA, 2017.
[51] T. O. Raubenheimer, Technical Report LCLSII-1.1-DR-0251-R0, USA, 2015.
[52] J. Duris, A. Murokh, and P. Musumeci, New J. Phys. **17**, 063036 (2015).
[53] A. Mak, F. Curbis, and S. Werin, Phys. Rev. ST Accel. Beams **18**, 040702 (2015).
[54] A. Halavanau, F.-J. Decker, C. Emma, J. Sheppard, and C. Pellegrini, J. Synchrotron Radiat. **26**, 635 (2019).
[55] K.-J. Kim and Y. V. Shvyd'ko, Phys. Rev. ST Accel. Beams **12**, 030703 (2009).
[56] K.-J. Kim, Y. Shvyd'ko, and S. Reiche, Phys. Rev. Lett. **100**, 244802 (2008).
[57] J. Goodman, *Introduction to Fourier Optics*, Electrical Engineering Series (McGraw-Hill, New York, 1996).
[58] Y. Shvyd'ko and R. Lindberg, Phys. Rev. ST Accel. Beams **15**, 100702 (2012).
[59] K. L. F. Bane and M. Sands, AIP Conf. Proc. **367**, 131 (1996).
[60] W. Qin, S. Huang, K. Liu, K.-J. Kim, R. Lindberg, Y. Ding, Z. Huang, T. Maxwell, K. Bane, and G. Marcus, in *38th International Free-Electron Laser Conference (FEL'17), New Mexico, USA, 2017* (Joint Accelerator Conferences Website (JACoW), 2017), pp. 247–250.
[61] R. W. Schoenlein, S. Boutet, M. P. Minitti, and A. M. Dunne, Appl. Sci. **7**, 850 (2017).